Accurate determination of the 3D atomic structure of amorphous materials

https://doi.org/10.1038/s41586-025-09857-4

Received: 15 June 2025

Accepted: 4 November 2025

Published online: 28 January 2026

Check for updates

Yuxuan Liao[1], Haozhi Sha[1], Colum M. O'Leary[1], Hanfeng Zhong[1], Yao Yang[2] & Jianwei Miao[1]✉

Amorphous materials—solids lacking long-range order—underpin technologies from thin-film electronics[1], solar cells[2] and phase-change memory[3] to magnetic components[4], medical devices[5] and quantum technologies[6–8]. Yet the absence of periodicity fundamentally limits determination of their three-dimensional (3D) structure at atomic resolution. Despite major theoretical, experimental, and computational advances in characterizing short- and medium-range order[9–24], quantitative determination of complete 3D atomic arrangements in amorphous materials remains experimentally demanding. Atomic electron tomography (AET) now provides a pathway to direct 3D atomic mapping in these materials[25–27]. Here we present a quantitative analysis of AET, showing how robust image preprocessing, denoising, projection alignment and normalization, advanced tomographic reconstruction, atom tracing, elemental classification and atomic position refinement collectively enable reliable determination of 3D atomic coordinates and elemental identities in amorphous materials. Using multislice-simulated datasets of amorphous Si, SiGeSn and CoPdPt nanoparticles under varying noise levels, our workflow outperforms an alternative approach[28] in both positional precision and classification accuracy. For CoPdPt, we identify 95.1% of Co, 99.0% of Pd and 100% of Pt atoms, with corresponding 3D positional precisions of 29 pm, 12 pm and 6 pm, respectively, under realistic dose conditions. These results establish practical guidelines and quantitative benchmarks for achieving accurate AET of non-crystalline materials, and the underlying framework can be broadly applied to other tomographic imaging modalities for high-fidelity 3D reconstruction.

Atomic electron tomography (AET) combines advanced electron microscopy techniques with powerful computational methods to determine the three-dimensional (3D) structure of materials at the single-atom level[27,29]. Since its first experimental demonstration in 2012 (ref. 30), AET has been extended to resolve 3D atomic arrangements across a broad range of material systems, including nanoparticles[31–34], needle-shaped samples[35], two-dimensional (2D) materials[36,37], medium- and high-entropy nanoalloys[38], nanocatalysts[39–41] and, most notably, amorphous solids[25,26]. Unlike crystallography or cryo-electron microscopy, AET does not require crystallinity or rely on averaging over many identical structures, enabling quantitative 3D imaging of individual, non-periodic structures. Despite these advances, AET remains technically demanding: accurate 3D atomic reconstruction depends critically on every stage of the workflow, including image preprocessing, noise suppression, background correction, angular calibration, projection alignment and normalization, optimized tomographic reconstruction, and accurate atom tracing and refinement. In practice, small deviations in these steps can propagate into systematic errors in atomic coordinates and elemental identification, limiting reproducibility and quantitative interpretation. Here we present a comprehensive analysis of the AET framework, identifying the key computational and algorithmic factors that govern accuracy and demonstrating a robust workflow for determining reliable 3D atomic coordinates and chemical identities in amorphous materials.

The AET framework

Table 1 summarizes the AET workflow for preprocessing, tomographic reconstruction and postprocessing, alongside the corresponding procedures used in ref. 28 for comparison. Our approach makes only minimal previous assumptions—atomicity, minimum interatomic spacing and known chemical species—ensuring model-independent and unbiased structural determination. To benchmark its performance, we simulated tomographic tilt series from two amorphous Si nanoparticles containing 208 and 19,993 atoms, respectively, as reported in ref. 28. Each annular dark-field scanning transmission electron microscopy (ADF-STEM) projection was generated using the multislice method in abTEM[42] with eight frozen phonons to account for thermal vibrations at room temperature. All simulation parameters were carefully optimized to ensure accurate wave propagation and faithful preservation of high-angle scattering, as detailed in Extended Data Table 1. A random defocus variation of ±3 nm was applied to emulate

[1]Department of Physics and Astronomy and California NanoSystems Institute, University of California, Los Angeles, CA, USA. [2]School of Engineering, Westlake University, Hangzhou, China. ✉e-mail: j.miao@ucla.edu

Table 1 | Comparison of methods and procedures used in this study and in ref. 28

		This study	Reference 28
Projection simulation, background addition, and noise modelling	Projection simulation	Multislice simulations (abTEM[42]) are performed with the electron beam focused at the centre of the sample, consistent with experimental conditions. A random defocus shift of ±3 nm was applied to emulate experimental uncertainties.	Absorptive-potential projection method (Eqs. 1–2 in their paper) with a fixed defocus of −5 nm
	Probe partial coherence	Convolution with a 0.35 Å Gaussian kernel	-
	Background	1 e^- per pixel	1 e^- per pixel
	Noise	Poisson noise added to simulated projections; workflow also supports Poisson and Gaussian noise for experimental data; scan noise not included	Poisson noise added to simulated projections; scan noise not included
Preprocessing	Denoising method	1. Estimate Gaussian–Poisson noise parameters for each projection. 2. Apply forward variance-stabilizing transformation (VST). 3. Rescale projection intensity to the [0, 1] range. 4. Apply BM3D denoising algorithm[43]. 5. Apply inverse VST. 6. Rescale projection intensity back to original values.	1. Blur the point spread function and apply an image filter. 2. Deblur using iterative VST and coloured noise removal. 3. Apply a Butterworth low-pass filter. 4. Rescale projection intensity to [0, 1]. 5. Apply a Gaussian filter (σ=1). 6. Rescale projection intensity to [0, 1].
	Background subtraction	Laplacian and threshold method[25] 1. Use Otsu's method (MATLAB) to determine an intensity threshold. 2. Create a binary mask for each projection. 3. Smooth the mask with an edge-preserving filter. 4. Zero out values outside the mask. 5. Estimate and subtract the background within the mask using the Laplacian (regionfill in MATLAB).	–
	Projection alignment and normalization	Centre-of-mass and common-line alignment[30,31]	Use a few heavy atoms as fiducial markers for alignment.
Tomographic reconstruction	Initial reconstruction	RESIRE[44]: each voxel was subdivided into 2×2×2 elements to achieve sub-voxel resolution in real space	Updated SIRT: Input projections are interpolated at an oversampling ratio of 3
	Reconstruction refinement	RESIRE further refines alignment, normalization, background subtraction, and tilt-angle correction via back-projection, with convergence monitored by an R-factor[44].	–
Postprocessing	Atom tracing	Polynomial fitting[33,56]	Polynomial fitting[33,56]
	Elemental classification	*K*-means clustering[33,57]	*K*-means clustering[33,57]
	3D atomic coordinate refinement	The 3D atomic coordinates are refined by minimizing the discrepancy between denoised and calculated projections.	–

experimental focusing conditions, and each projection was convolved with a 0.35 Å Gaussian kernel to model partial coherence. Poisson noise was added to simulate electron doses of 8×10^3 e^- Å^{-2}, 1.6×10^4 e^- Å^{-2} and 1.6×10^5 e^- Å^{-2} for both nanoparticles. A constant background of 1 e^- per pixel was also included, corresponding to 26 and 8 e^- Å^{-2} for the smaller and larger nanoparticles, respectively, due to their different pixel sizes. For consistency with ref. 28, all reported dose values refer to the dose per projection. Figure 1a shows a representative ADF-STEM projection of the 208-atom amorphous Si nanoparticle at a dose of 1.6×10^4 e^- Å^{-2}, illustrating substantial background signal and Poisson noise.

After applying block-matching and 3D filtering[43] to denoise the projections and using the Laplacian and threshold method for background subtraction[25] (Fig. 1b), we reconstructed the 3D structures of the two amorphous Si nanoparticles using the real-space iterative reconstruction (RESIRE) algorithm[44]. The reconstruction process consisted of an initial volume generation followed by iterative refinement (Table 1). Figure 1c shows a representative projection of the 208-atom Si nanoparticle calculated from the final 3D reconstruction. After postprocessing, all 208 Si atoms were correctly traced with a positional precision of 17 pm, quantified by the root-mean-square deviation between the traced and ground-truth atomic models. At electron doses of 8×10^3 e^- Å^{-2} and 1.6×10^5 e^- Å^{-2}, 199 atoms (95.7%) and 208 atoms (100%) were accurately identified, with corresponding 3D positional precisions of 29 pm and 4 pm, respectively (Fig. 1d and Extended Data Figs. 1a–f and 2a–c). For the 19,993-atom amorphous Si nanoparticle, we observed similar dose-dependent improvements in both atom identification and positional precision: from 92.3% (39 pm) at 8×10^3 e^- Å^{-2} to 98.2% (25 pm) at 1.6×10^4 e^- Å^{-2}, reaching 100% (12 pm) at 1.6×10^5 e^- Å^{-2} (Fig. 1h). Representative projections and atomic identification results are shown in Fig. 1e–g and Extended Data Figs. 1g–l and 2d–f. Our workflow achieves consistently higher precision and accuracy than that reported in ref. 28, which failed to reconstruct atomic models at doses below 1.0×10^4 e^- Å^{-2}.

To enable a direct comparison, we reconstructed the 208-atom amorphous Si nanoparticle using our AET framework and the same ADF-STEM projections (dose: 6.6×10^4 e^- Å^{-2}) reported in ref. 28, which did not include a random defocus range or a 0.35 Å Gaussian convolution to model partial coherence (Extended Data Fig. 3). After preprocessing, an initial 3D reconstruction was generated using the RESIRE algorithm[44], followed by refined background subtraction through comparison between the calculated and denoised projections. The final

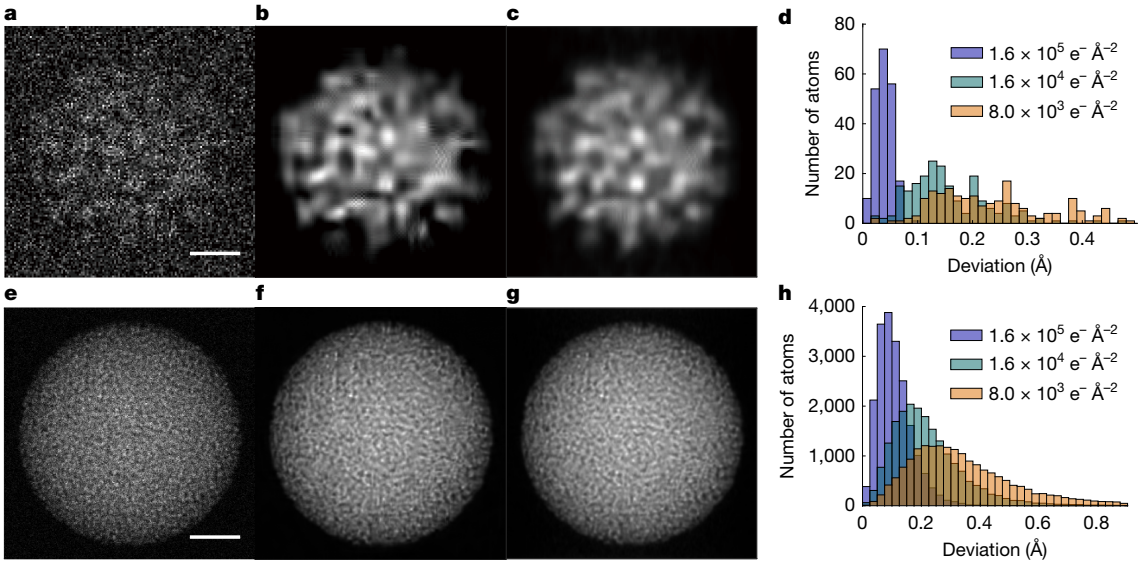

Fig. 1 | Improved 3D reconstruction and atom tracing of 208-atom and 19,993-atom amorphous Si nanoparticles using our AET workflow. **a**, Representative projection of the 208-atom nanoparticle at a dose of 1.6×10^4 e^- Å^{-2}. Scale bar, 5 Å. **b**, Denoised and background-subtracted projection, showing residual artefacts due to low signal-to-noise ratio. **c**, Corresponding projection calculated from the RESIRE reconstruction. **d**, 3D positional precision of correctly identified atoms in the 208-atom nanoparticle: 29 pm, 17 pm and 4 pm for doses of 8×10^3 e^- Å^{-2}, 1.6×10^4 e^- Å^{-2} and 1.6×10^5 e^- Å^{-2}, respectively. **e**–**g**, Same as **a**–**c** for the 19,993-atom nanoparticle at a dose of 1.6×10^4 e^- Å^{-2}. Scale bar, 2 nm. **h**, 3D positional precision for the 19,993-atom nanoparticle: 39 pm, 25 pm and 12 pm for the same three dose levels.

3D volume was then traced to produce the atomic model (Extended Data Fig. 3d). All 208 Si atoms were correctly identified with a 3D positional precision of 5 pm (Extended Data Fig. 3e), representing more than a two-fold improvement over the precision reported in ref. 28. These results highlight the importance of rigorous denoising and background subtraction in AET, as omitting these steps can markedly reduce atom-identification accuracy and 3D positional precision.

Three-dimensional atomic localization and classification

Apart from proper denoising and background subtraction, accurate alignment and intensity normalization are essential for high-quality AET reconstructions. Even sub-ångström misalignments can introduce cumulative artefacts that degrade atomic positional precision and elemental identification. To illustrate their importance, we reconstructed an amorphous SiGeSn nanoparticle using the simulated projections at a dose of 1.6×10^4 e^- Å^{-2} reported in ref. 28. Applying the centre-of-mass and common-line methods to these projections[29,30] revealed both projection misalignment and intensity mis-normalization (Extended Data Fig. 4a,b). After realignment and renormalization (Extended Data Fig. 4c), we performed 3D reconstruction using the RESIRE algorithm[44], obtaining improved atomic localization compared with the reconstruction in ref. 28 (Extended Data Fig. 4d,e). Postprocessing of the RESIRE reconstruction further showed that elemental identification of Si, Ge and Sn atoms in our AET workflow agrees closely with the ground truth (Extended Data Fig. 4f), whereas ref. 28 overestimated the number of Si atoms by 48% (Extended Data Fig. 4g).

To perform more rigorous simulations of the SiGeSn nanoparticle, we used the multislice method[42] to calculate projections incorporating eight frozen phonons (Extended Data Table 1). Each projection was convolved with a 0.35 Å Gaussian kernel to model partial coherence and then superimposed with a constant background and Poisson noise at electron doses of 1.6×10^4 e^- Å^{-2} and 1.6×10^5 e^- Å^{-2}. The resulting tilt series were preprocessed, reconstructed using the RESIRE algorithm[44] and analysed for individual atomic positions (Fig. 2a–c). Figure 2d,e shows that elemental identification rates improved from 61.3% to 75.1% for Si, 99.0% to 99.9% for Ge and remained 100% for Sn, whereas 3D positional precisions improved from 68 pm to 50 pm (Si), 18 pm to 10 pm (Ge) and 9 pm to 5 pm (Sn) as the dose increased from 1.6×10^4 e^- Å^{-2} to 1.6×10^5 e^- Å^{-2} (Fig. 2f). The lower precision for Si atoms is attributed to their reduced Z-contrast in ADF-STEM imaging.

Next, we re-examined the reconstruction of the amorphous CoPdPt nanoparticle reported in ref. 28 and identified substantial projection misalignment and intensity mis-normalization (Extended Data Fig. 5a,b). We measured lateral shifts of −0.92 Å to 1.25 Å perpendicular to the tilt axis, which are substantially larger than the shifts in the SiGeSn projections (−0.45 Å to 0.11 Å; Extended Data Fig. 4a). After realignment and renormalization of the projections (Extended Data Fig. 5c), we performed a RESIRE reconstruction, which yielded a more accurate 3D atomic structure and a clearer separation of atomic species in the histogram compared with the reconstruction in ref. 28 (Extended Data Fig. 5d–g). From our RESIRE reconstruction, we identified 89.5% of Co, 73.7% of Pd and 97.6% of Pt atoms, with corresponding 3D positional precisions of 39 pm, 11 pm and 8 pm (Extended Data Fig. 5g). By contrast, using the reconstruction from ref. 28, we identified only 45.7% of Co, 52.7% of Pd and 76.2% of Pt atoms, with corresponding 3D positional precisions of 98 pm, 79 pm and 49 pm (Extended Data Fig. 5f). These identification rates are consistent with those reported in ref. 28 (40% Co, 55% Pd and 84% Pt), although the corresponding 3D positional precision values were not reported. Collectively, these results, together with additional analysis (Methods), demonstrate that the substantial projection misalignment and intensity mis-normalization in the dataset of ref. 28 directly caused inaccurate atom identification and elemental classification (Extended Data Fig. 5).

Moreover, we identified two anomalies in Extended Data Fig. 5g: (1) Co atoms were detected at a higher percentage than the heavier Pd atoms, contrary to the expected Z-contrast behaviour in ADF-STEM imaging; and (2) the intensity distribution of Pt atoms exhibited a bimodal profile. We attribute both anomalies to the specific simulation and preprocessing procedures used in ref. 28 to generate the noisy CoPdPt projections (Table 1). To address these issues, we recalculated the projections of the same amorphous CoPdPt nanoparticle using the multislice method[42] with eight frozen phonons (Fig. 3a and Extended Data Table 1). This fully dynamical simulation, which captures multiple scattering and thermal-diffuse effects, is more accurate and physically

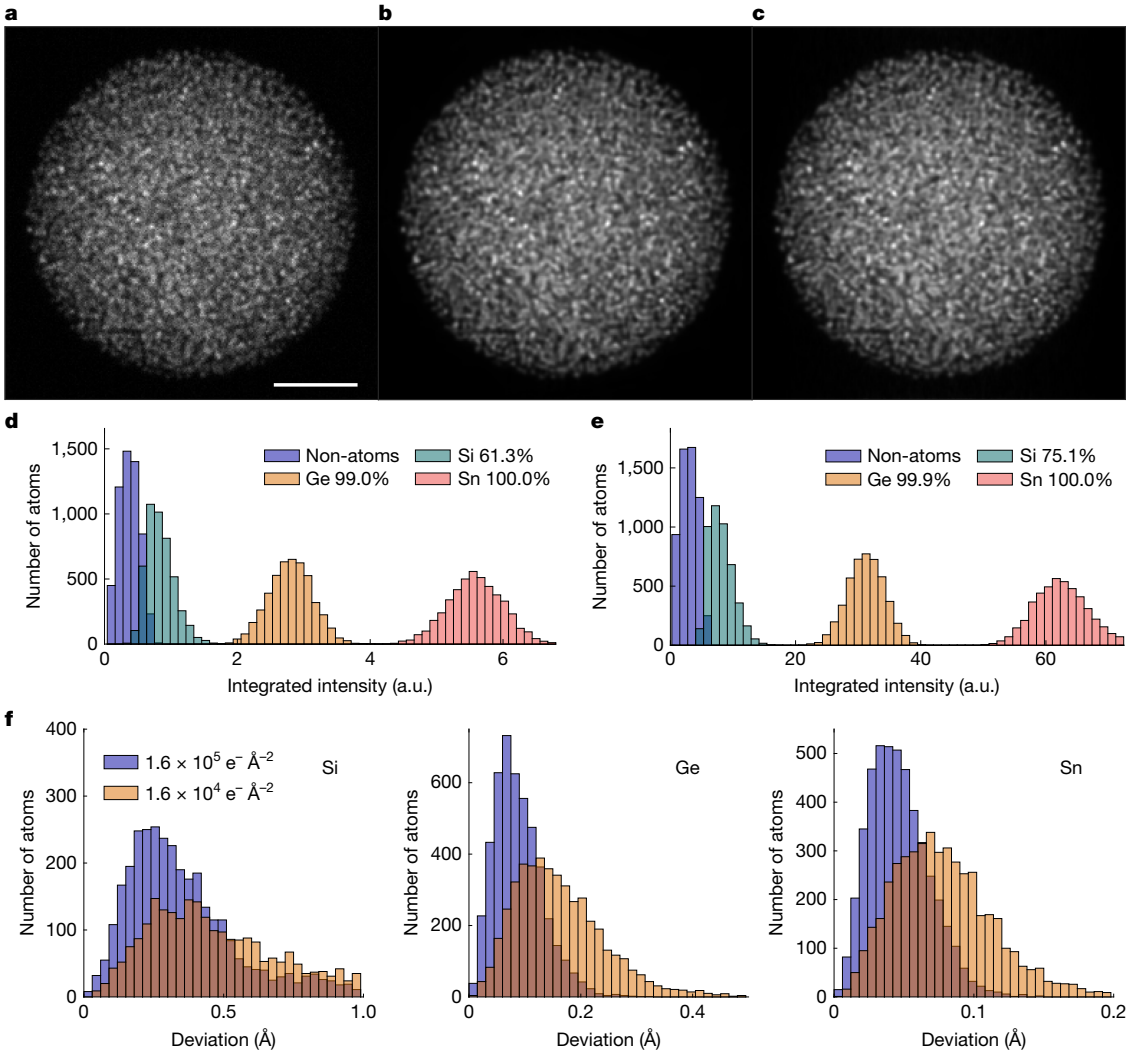

Fig. 2 | Three-dimensional atomic localization and elemental identification of a 13,982-atom amorphous SiGeSn nanoparticle using our AET workflow. **a**, Representative projection at a dose of 1.6×10^4 e^- Å^{-2}. Scale bar, 2 nm. **b**, Denoised and background-subtracted projection. **c**, Corresponding projection calculated from the RESIRE reconstruction. **d**,**e**, Histograms of traced Si, Ge and Sn atoms at doses of 1.6×10^4 e^- Å^{-2} (**d**) and 1.6×10^5 e^- Å^{-2} (**e**), with correct identification improving from 61.3% to 75.1% (Si), 99.0% to 99.9% (Ge) and remaining at 100% (Sn). Overall identification accuracy increases from 86.9% to 91.8%. **f**, 3D positional precision improves from 68 pm to 50 pm (Si), 18 pm to 10 pm (Ge) and 9 pm to 5 pm (Sn) at the two doses, with overall precision improving from 35 pm to 27 pm. a.u., arbitrary units.

rigorous than the absorptive-potential projection method in ref. 28. The electron probe was focused at the centre of the nanoparticle to better reproduce the experimental conditions, in contrast to the −5 nm defocus used in ref. 28. Each projection was then convolved with a 0.35 Å Gaussian kernel to model partial coherence, followed by the addition of a 1 e^- per pixel background (equivalent to 8 e^- Å^{-2}) and Poisson noise at a dose of 1.7×10^4 e^- Å^{-2}, consistent with the experimental parameters[25].

After projection denoising and background subtraction (Fig. 3b), we reconstructed the 3D volume using the RESIRE algorithm[44] (Fig. 3c), followed by atom tracing and elemental classification. The resulting histogram of traced atoms (Fig. 3d) shows well-separated peaks for each element, with no splitting of the Pt peak. Based on this histogram, we correctly identified 95.1% of Co, 99.0% of Pd and 100% of Pt atoms, with 3D positional precisions of 29 pm, 12 pm and 6 pm, respectively (Fig. 3e). The overall identification accuracy was 97.4%, with a mean 3D positional precision of 21 pm, consistent with the previously estimated experimental precision[25]. To evaluate the effect of defocus errors, we repeated the same procedure while introducing a random defocus variation of ±3 nm to simulate experimental uncertainties. Extended Data Fig. 6 shows that the identification accuracy and 3D precision decreased by 2.4% and 7 pm, respectively, highlighting the importance of minimizing defocus variations during data acquisition. Overall, these results represent a substantial improvement over those reported in ref. 28 and underscore the necessity of a systematic workflow for generating accurate 3D atomic models.

Another key development in AET has been the advancement of tomographic reconstruction algorithms. Although both direct inversion and iterative methods were already established in electron tomography[45], an important advance came in 2005 with the introduction of the oversampling principle, originally developed for phase retrieval in coherent diffractive imaging[46], into tomographic reconstruction[47]. Because tomographic reconstruction involves transforming data from polar to Cartesian coordinates, it inherently introduces interpolation errors. Oversampling in either real or reciprocal space mitigates this intrinsic imprecision compared with non-oversampled reconstructions under the same interpolation scheme, albeit at the cost of increased computational demand. Subsequent numerical and experimental studies demonstrated that iterative algorithms incorporating oversampling consistently outperform conventional tomographic methods[44,48]. Moreover, these algorithms include iterative refinements for background subtraction, projection alignment, intensity normalization and tilt-angle correction, with convergence quantitatively monitored using

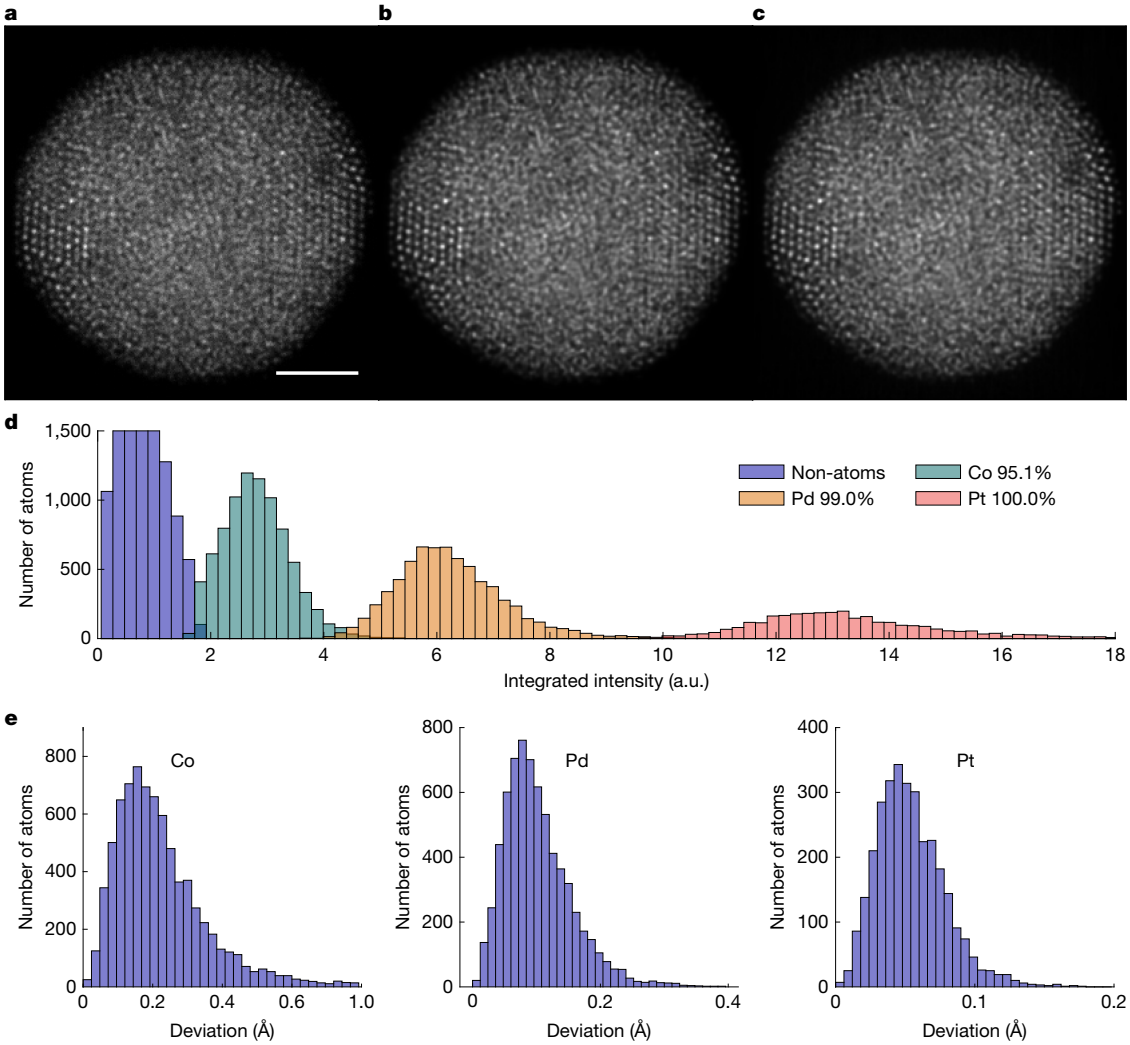

Fig. 3 | Three-dimensional atomic localization and elemental identification of an 18,356-atom amorphous CoPdPt nanoparticle using our AET workflow. **a**, Representative projection simulated with the electron probe focused at the nanoparticle centre and a dose of 1.7×10^4 $e^- Å^{-2}$, matching experimental conditions[25]. Scale bar, 2 nm. **b**, Denoised and background-subtracted projection. **c**, Corresponding projection calculated from the RESIRE reconstruction. **d**, Histogram of traced atoms showing identification accuracies of 95.1% (Co), 99.0% (Pd), and 100% (Pt), with an overall accuracy of 97.4%. **e**, 3D positional precisions of 29 pm (Co), 12 pm (Pd), and 6 pm (Pt); overall precision, 21 pm.

an R-factor defined as the normalized difference between calculated and measured projections.

To demonstrate the effectiveness of these advanced algorithms, we used RESIRE[44], the latest development in this class of methods, to reconstruct multislice-simulated noisy projections of the amorphous CoPdPt nanoparticle at a dose of 1.7×10^4 $e^- Å^{-2}$ with tilt-angle errors (Extended Data Fig. 7a). For comparison, we applied the updated simultaneous iterative reconstruction technique (SIRT) used in ref. 28 to the same tilt series. Although this version incorporates the oversampling principle and improves on conventional SIRT[49], it lacks angular correction and other iterative refinement features implemented in RESIRE (Table 1). Using RESIRE with angular correction, we correctly identified 94.8% of Co, 98.9% of Pd and 100% of Pt atoms, with 3D positional precisions of 30 pm, 12 pm and 7 pm, respectively (Extended Data Fig. 7b). Even without angular correction, RESIRE achieved identification accuracies and precisions of 87.1% and 42 pm for Co, 95.5% and 17 pm for Pd and 99.7% and 9 pm for Pt, still outperforming the updated SIRT method, which yielded 85.8% and 44 pm for Co, 95.7% and 19 pm for Pd and 99.7% and 12 pm for Pt (Extended Data Fig. 7c,d). These results demonstrate that RESIRE achieves both higher elemental identification accuracy and greater 3D atomic positional precision than the updated SIRT algorithm[28] under experimentally realistic conditions.

Three-dimensional atomic structure determination by pAET

Compared with ADF-STEM, electron ptychography is a coherent imaging method that records both unscattered and scattered components of the transmitted wave, resulting in higher dose efficiency[27]. When combined with AET, termed pAET, it enables high-precision 3D atomic imaging under practical dose conditions[50,51]. To demonstrate this ability, we simulated a 6 nm amorphous silica nanoparticle generated by molecular dynamics and calculated diffraction patterns using the multislice method[42] with an 80 keV probe and eight frozen phonons (Extended Data Table 1). Two tilt series were simulated at doses of 1.6×10^3 $e^- Å^{-2}$ and 1.6×10^4 $e^- Å^{-2}$. Multislice and single-slice ptychography[27,52–54] were applied to reconstruct the complex object and probe functions (Extended Data Table 2). Building on the ankylography concept of single-view 3D structure determination introduced in 2010 (ref. 55), multislice ptychography leverages coherent scattering and the curvature of the Ewald sphere to encode depth information in 2D diffraction patterns, achieving higher reconstruction fidelity than the single-slice approach. Each reconstructed projection was convolved with a 0.35 Å Gaussian kernel to account for partial coherence before 3D reconstruction. At 1.6×10^3 $e^- Å^{-2}$, multislice pAET

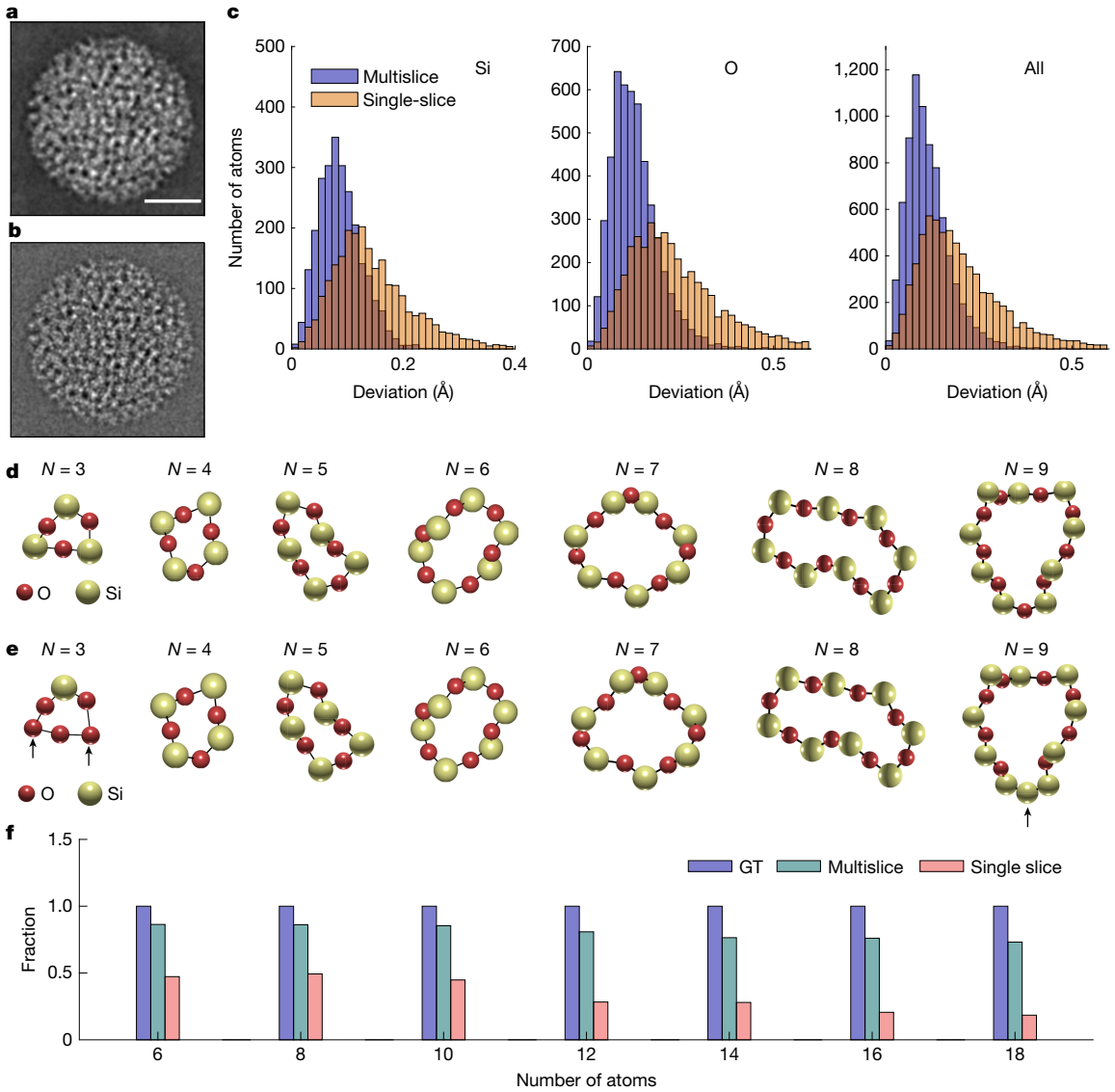

Fig. 4 | Three-dimensional atomic structure and medium-range order of a 7,704-atom amorphous silica nanoparticle reconstructed by pAET (dose 1.6×10^3 e$^-$ Å^{-2}). a,**b**, Representative projections reconstructed by single-slice (**a**) and multislice (**b**) ptychography. Scale bar, 2 nm. **c**, Atom-identification rates: 90.8% (Si), 77.5% (O) and 82% (all atoms) for single-slice pAET; 98.2% (Si), 96.7% (O) and 97.2% (all atoms) for multislice pAET. Corresponding 3D positional precisions: 17 pm (Si), 28 pm (O) and 24 pm (all atoms) for single-slice; 10 pm (Si), 14 pm (O) and 13 pm (all atoms) for multislice. **d**, Seven representative *N*-membered atomic rings in the ground-truth structure. **e**, Corresponding *N*-membered rings from multislice pAET, with homopolar defects indicated by arrows. **f**, Heteroatomic ring-size distributions from the ground truth, single-slice and multislice pAET.

improved atom-identification accuracy from 82% to 97.2% and 3D precision from 24 pm to 13 pm relative to single-slice pAET (Fig. 4a–c). At 1.6×10^4 e$^-$ Å^{-2}, multislice pAET achieved 100% accuracy and 7 pm precision, whereas single-slice reached 88.8% and 19 pm (Extended Data Fig. 8a).

Accurate localization of individual Si and O atoms enables quantitative analysis of medium-range order in amorphous silica. According to the model in ref. 9, alternating Si–O rings define the glass network topology. Using multislice pAET at 1.6×10^3 e$^-$ Å^{-2}, 80.6% of identified rings preserved correct heteroatomic ordering, compared with 33.8% for single-slice reconstructions (Fig. 4d–f). At 1.6×10^4 e$^-$ Å^{-2}, multislice pAET fully recovered the heteroatomic network without homopolar defects (Extended Data Fig. 8b). Despite its potential, pAET remains experimentally demanding for imaging light elements in amorphous materials. The main challenges are (1) mitigating radiation damage in low-Z materials; (2) maintaining consistent multislice ptychographic reconstructions across all tilt angles; and (3) accurately aligning noisy phase projections under experimental uncertainties.

Conclusions

We present a comprehensive and quantitative framework for accurately determining the 3D atomic structure of amorphous materials. By integrating robust preprocessing, advanced tomographic reconstruction and systematic postprocessing, our AET workflow enables reliable determination of 3D atomic coordinates and elemental identities across diverse disordered systems. Benchmarking against ref. 28 shows substantial improvements in both 3D positional precision and elemental classification accuracy. Rigorous numerical simulations further demonstrate that pAET can resolve the 3D atomic structure and medium-range order of amorphous silica under realistic dose conditions. Each stage of the workflow, from denoising, background subtraction and projection alignment to normalization, angular correction, tomographic reconstruction, atomic tracing and position refinement, contributes to the fidelity and quantitative precision of the final 3D atomic model. Collectively, these results establish a quantitative foundation for AET and pAET by defining the conditions and workflow parameters required

for accurate 3D atomic reconstruction. Although simulations cannot fully capture experimental complexity, this analysis clarifies the capabilities and practical constraints of AET and pAET and, when combined with carefully executed experiments, is expected to enable reliable determination of 3D atomic structures in non-crystalline materials.

Online content

Any methods, additional references, Nature Portfolio reporting summaries, source data, extended data, supplementary information, acknowledgements, peer review information; details of author contributions and competing interests; and statements of data and code availability are available at https://doi.org/10.1038/s41586-025-09857-4.

1. Nomura, K. et al. Room-temperature fabrication of transparent flexible thin-film transistors using amorphous oxide semiconductors. *Nature* **432**, 488–492 (2004).
2. Carlson, D. E. & Wronski, C. R. Amorphous silicon solar cell. *Appl. Phys. Lett.* **28**, 671–673 (1976).
3. Wuttig, M., Bhaskaran, H. & Taubner, T. Phase-change materials for non-volatile photonic applications. *Nat. Photon.* **11**, 465–476 (2017).
4. Wang, W. H., Dong, C. & Shek, C. H. Bulk metallic glasses. *Mater. Sci. Eng. R Rep.* **44**, 45–89 (2004).
5. Li, H. F. & Zheng, Y. F. Recent advances in bulk metallic glasses for biomedical applications. *Acta Biomater.* **36**, 1–20 (2016).
6. Esmaeil Zadeh, I. et al. Superconducting nanowire single-photon detectors: a perspective on evolution, state-of-the-art, future developments, and applications. *Appl. Phys. Lett.* **118**, 190502 (2021).
7. Li, B. et al. Down-converted photon pairs in a high-Q silicon nitride microresonator. *Nature* **639**, 922–927 (2025).
8. de Leon, N. P. et al. Materials challenges and opportunities for quantum computing hardware. *Science* **372**, eabb2823 (2021).
9. Zachariasen, W. H. The atomic arrangement in glass. *J. Am. Chem. Soc.* **54**, 3841–3851 (1932).
10. Warren, B. E. & Biscob, J. Fourier analysis of X-ray patterns of soda-silica glass. *J. Am. Ceram. Soc.* **21**, 259–265 (1938).
11. Frank, F. C. Supercooling of liquids. *Proc. R. Soc. Lond. A* **215**, 43–46 (1952).
12. Bernal, J. D. Geometry of the structure of monatomic liquids. *Nature* **185**, 68–70 (1960).
13. Finney, J. L. Random packings and structure of simple liquids. I. The geometry of random close packing. *Proc. R. Soc. Lond. A* **319**, 479–493 (1970).
14. McGreevy, R. L. & Pusztai, L. Reverse Monte Carlo simulation: a new technique for the determination of disordered structures. *Mol. Simul.* **1**, 359–367 (1988).
15. Elliott, S. R. Medium-range structural order in covalent amorphous solids. *Nature* **354**, 445–452 (1991).
16. Kresse, G. & Hafner, J. *Ab initio* molecular-dynamics simulation of the liquid-metal–amorphous-semiconductor transition in germanium. *Phys. Rev. B* **49**, 14251–14269 (1994).
17. Kelton, K. F. et al. First X-ray scattering studies on electrostatically levitated metallic liquids: demonstrated influence of local icosahedral order on the nucleation barrier. *Phys. Rev. Lett.* **90**, 195504 (2003).
18. Miracle, D. B. A structural model for metallic glasses. *Nat. Mater.* **3**, 697–702 (2004).
19. Sheng, H. W., Luo, W. K., Alamgir, F. M., Bai, J. M. & Ma, E. Atomic packing and short-to-medium-range order in metallic glasses. *Nature* **439**, 419–425 (2006).
20. Cheng, Y. Q. & Ma, E. Atomic-level structure and structure-property relationship in metallic glasses. *Prog. Mater Sci.* **56**, 379–473 (2011).
21. Hwang, J. et al. Nanoscale structure and structural relaxation in $Zr_{50}Cu_{45}A_{15}$ bulk metallic glass. *Phys. Rev. Lett.* **108**, 195505 (2012).
22. Treacy, M. M. J. & Borisenko, K. B. The local structure of amorphous silicon. *Science* **335**, 950–953 (2012).
23. Hirata, A. et al. Geometric frustration of icosahedron in metallic glasses. *Science* **341**, 376–379 (2013).
24. Lan, S. et al. A medium-range structure motif linking amorphous and crystalline states. *Nat. Mater.* **20**, 1347–1352 (2021).
25. Yang, Y. et al. Determining the three-dimensional atomic structure of an amorphous solid. *Nature* **592**, 60–64 (2021).
26. Yuan, Y. et al. Three-dimensional atomic packing in amorphous solids with liquid-like structure. *Nat. Mater.* **21**, 95–102 (2022).
27. Miao, J. Computational microscopy with coherent diffractive imaging and ptychography. *Nature* **637**, 281–295 (2025).
28. Busch, R., Rez, P., Treacy, M. M. J. & Zuo, J.-M. Limit of atomic resolution tomography reconstruction of amorphous nanoparticles. *Nature* https://doi.org/10.1038/s41586-025-09924-w (2026).
29. Miao, J., Ercius, P. & Billinge, S. J. L. Atomic electron tomography: 3D structures without crystals. *Science* **353**, aaf2157 (2016).
30. Scott, M. C. et al. Electron tomography at 2.4-ångström resolution. *Nature* **483**, 444–447 (2012).
31. Chen, C.-C. et al. Three-dimensional imaging of dislocations in a nanoparticle at atomic resolution. *Nature* **496**, 74–77 (2013).
32. Goris, B. et al. Measuring lattice strain in three dimensions through electron microscopy. *Nano Lett.* **15**, 6996–7001 (2015).
33. Yang, Y. et al. Deciphering chemical order/disorder and material properties at the single-atom level. *Nature* **542**, 75–79 (2017).
34. Zhou, J. et al. Observing crystal nucleation in four dimensions using atomic electron tomography. *Nature* **570**, 500–503 (2019).
35. Xu, R. et al. Three-dimensional coordinates of individual atoms in materials revealed by electron tomography. *Nat. Mater.* **14**, 1099–1103 (2015).
36. Tian, X. et al. Correlating the three-dimensional atomic defects and electronic properties of two-dimensional transition metal dichalcogenides. *Nat. Mater.* **19**, 867–873 (2020).
37. Tian, X. et al. Capturing 3D atomic defects and phonon localization at the 2D heterostructure interface. *Sci. Adv.* **7**, eabi6699 (2021).
38. Moniri, S. et al. Three-dimensional atomic structure and local chemical order of medium and high-entropy nanoalloys. *Nature* **624**, 564–569 (2023).
39. Jo, H. et al. Direct strain correlations at the single-atom level in three-dimensional core–shell interface structures. *Nat. Commun.* **13**, 5957 (2022).
40. Li, Z. et al. Probing the atomically diffuse interfaces in Pd@Pt core–shell nanoparticles in three dimensions. *Nat. Commun.* **14**, 2934 (2023).
41. Yang, Y. et al. Atomic-scale identification of the active sites of oxygen reduction nanocatalysts. *Nat. Catal.* **7**, 796–806 (2024).
42. Madsen, J. & Susi, T. The abTEM code: transmission electron microscopy from first principles. *Open Res. Eur.* **1**, 24 (2021).
43. Dabov, K., Foi, A., Katkovnik, V. & Egiazarian, K. Image Denoising by Sparse 3-D Transform-Domain Collaborative Filtering. *IEEE Trans. Image Process.* **16**, 2080–2095 (2007).
44. Pham, M., Yuan, Y., Rana, A., Osher, S. & Miao, J. Accurate real space iterative reconstruction (RESIRE) algorithm for tomography. *Sci Rep.* **13**, 5624 (2023).
45. Weyland, M. & Midgley, P. A. Electron tomography. *Mater. Today* **7**, 32–40 (2004).
46. Miao, J., Charalambous, P., Kirz, J. & Sayre, D. Extending the methodology of X-ray crystallography to allow imaging of micrometre-sized non-crystalline specimens. *Nature* **400**, 342–344 (1999).
47. Miao, J., Förster, F. & Levi, O. Equally sloped tomography with oversampling reconstruction. *Phys. Rev. B* **72**, 052103 (2005).
48. Pryor, A. Jr et al. GENFIRE: a generalized Fourier iterative reconstruction algorithm for high-resolution 3D imaging. *Sci Rep.* **7**, 10409 (2017).
49. Gilbert, P. Iterative methods for the three-dimensional reconstruction of an object from projections. *J. Theor. Biol.* **36**, 105–117 (1972).
50. Chang, D. J. et al. Ptychographic atomic electron tomography: Towards three-dimensional imaging of individual light atoms in materials. *Phys. Rev. B* **102**, 174101 (2020).
51. Pelz, P. M. et al. Solving complex nanostructures with ptychographic atomic electron tomography. *Nat. Commun.* **14**, 7906 (2023).
52. Maiden, A. M., Humphry, M. J. & Rodenburg, J. M. Ptychographic transmission microscopy in three dimensions using a multi-slice approach. *J. Opt. Soc. Am. A* **29**, 1606–1614 (2012).
53. Chen, Z. et al. Electron ptychography achieves atomic-resolution limits set by lattice vibrations. *Science* **372**, 826–831 (2021).
54. O'Leary, C. M. et al. Three-dimensional structure of buried heterointerfaces revealed by multislice ptychography. *Phys. Rev. Appl.* **22**, 014016 (2024).
55. Raines, K. S. et al. Three-dimensional structure determination from a single view. *Nature* **463**, 214–217 (2010).
56. Rogers, S. S., Waigh, T. A., Zhao, X. & Lu, J. R. Precise particle tracking against a complicated background: polynomial fitting with Gaussian weight. *Phys. Biol.* **4**, 220 (2007).
57. Lloyd, S. Least squares quantization in PCM. *IEEE Trans. Inf. Theory* **28**, 129–137 (1982).

Methods

Multislice simulations

The ground-truth atomic models of the amorphous Si, SiGeSn and CoPdPt nanoparticles were obtained from the references listed in Extended Data Table 1, whereas the SiO_2 model was generated by molecular dynamics simulation. The atomic coordinates were provided as input to the ab initio transmission electron microscopy (abTEM) package[42] and rotated to the desired angle of a single projection. The simulation volume of the nanoparticle was padded in three dimensions to avoid edge artefacts. The projected potentials for the simulation volume were calculated using the parameters provided in Extended Data Table 1. Eight frozen phonons were generated to account for atomic thermal vibrations during electron transmission at room temperature.

The images were generated in abTEM[42] using the multislice method to account for multiple electron scattering through the sample thickness[58,59]. The probe was calculated based on a convergence angle defined by a simulated aperture and was focused at the centre of the nanoparticle. A random focus shift of ±3 nm was applied to emulate operator-induced defocus variation during microscope alignment. The initial exit wave was computed by modelling the interaction between the incident electron probe and the first potential slice using the phase-object approximation. The resulting exit wave from each slice was used as the entrance wave for the next slice, and this process was repeated throughout the entire simulation volume. For each frozen phonon, the exit wave from the final slice was propagated to the detector plane by Fourier transform. The signal at each scan position was then calculated based on the specified detector geometry to generate either ADF-STEM images or a ptychography dataset (Extended Data Table 1). The ADF signal and diffraction pattern at each scan position were averaged over eight frozen phonons. The simulated ADF-STEM image was convolved with a 0.35 Å Gaussian kernel to account for partial coherence. A background noise of 1 e^- per pixel (corresponding to 26 e^- Å^{-2} and 8 e^- Å^{-2} for pixel sizes of 0.195 Å and 0.347 Å, respectively) was added, followed by Poisson noise to simulate a finite electron dose.

RESIRE reconstruction

RESIRE is a tomographic algorithm designed to achieve high-accuracy 3D reconstructions from a limited number of noisy 2D projections[44]. Unlike Fourier-based methods[47,48], RESIRE operates entirely in real space, incorporating the oversampling principle[46,60] and using gradient descent to iteratively minimize the difference between measured and calculated projections. It supports both Radon transform- and Fourier slice theorem-based forward projections, includes real-space constraints and features integrated angular refinement to correct tilt inaccuracies by minimizing the R-factor. Although both implementations achieve comparable accuracy, the Radon-based version is computationally more efficient, highly parallelizable and scalable to large datasets, completing 100 iterations in 36 s on three NVIDIA RTX A6000 GPUs. Benchmarking results show that RESIRE consistently outperforms conventional methods such as SIRT, filtered back-projection and generalized Fourier iterative reconstruction, particularly in scenarios involving missing wedges and/or angular errors[46]. Extended Data Table 1 lists the parameters used for RESIRE in this study. As the RESIRE source code for the Fourier slice version was made available at GitHub in ref. 25, the Radon-based version is provided alongside this paper (see Data availability).

Three-dimensional atomic position determination and elemental identification

Each reconstruction volume was oversampled by a factor of 3 in the *x*-, *y*-, and *z*-directions, and local maxima were identified. Starting from the highest-intensity peak, polynomial fitting[33,56] was applied to a 7 × 7 × 7 voxel region surrounding each maximum to determine its centre position—that is, the 3D coordinates of a potential atom. Peaks within 1 Å of each other were merged based on intensity. Finally, *K*-means clustering was used to exclude non-atomic sites and classify atomic species among the identified positions[33,57].

Assessment of histogram similarity and elemental classification

In ref. 28, the authors reported that the histogram of traced atom intensities in their simulated dataset (Extended Data Fig. 5f) was similar to the experimental histogram reported in ref. 25. However, our quantitative analysis demonstrates that the apparent similarity arises from projection misalignment and intensity mis-normalization introduced in the preprocessing of their reconstruction. First, the simulated CoPdPt dataset contains only three elements, whereas the experimental sample includes eight elements (Co, Ni, Ru, Rh, Pd, Ag, Ir and Pt) (ref. 25); therefore, the simulated histogram should exhibit more distinct peaks than the experimental one. Second, similar procedures were applied in ref. 28 to two compositionally distinct nanoparticles—an 8 nm amorphous SiGeSn and an 8 nm amorphous CoPdPt system. Although the SiGeSn histogram (Extended Data Fig. 4g) shows well-resolved intensity peaks for Si, Ge, and Sn, the CoPdPt histogram (Extended Data Fig. 5f) is substantially blurred, despite Co, Pd and Pt having higher atomic numbers and larger Z-contrast differences. This discrepancy is not consistent with physically expected contrast behaviour. Third, based on our extensive experience in AET over more than a decade of development and application, histograms derived from simulated data consistently show better peak separation than those obtained from experimental datasets, owing to the inherent variability and complexity of experimental conditions. The histogram similarity reported in ref. 28 is therefore unlikely to represent genuine physical correspondence.

Fourth, after applying the centre-of-mass and common-line methods[30,31] to the same projections used in ref. 28, we identified substantial projection misalignment and intensity mis-normalization (Extended Data Fig. 5a,b). Following realignment and renormalization of the projections (Extended Data Fig. 5c), RESIRE reconstruction yielded clearer separation of atomic species in the histogram and more accurate identification of Co, Pd and Pt atoms (Extended Data Fig. 5g). Finally, we analysed three simulated tomographic datasets provided in ref. 28: a 208-atom amorphous Si, a 13,982-atom amorphous SiGeSn and an 18,356-atom amorphous CoPdPt nanoparticle. We found no misalignment in the projections of the amorphous Si dataset, ruling out potential issues in their projection simulation code. In contrast, the SiGeSn dataset exhibited misalignment errors ranging from −0.45 Å to 0.11 Å (Extended Data Fig. 4a) and the CoPdPt dataset showed substantially larger misalignment errors ranging from −0.92 Å to 1.25 Å (Extended Data Fig. 5a). Collectively, these results demonstrate that the claims regarding histogram similarity and elemental classification in ref. 28 are not supported by quantitative analysis, and instead arise primarily from substantial projection misalignment and intensity mis-normalization introduced during their simulated data processing.

Electron ptychographic reconstruction

Single-slice and multislice electron ptychographic reconstructions were performed in MATLAB using the fold-slice package[53,61]. Single-slice ptychography models the specimen as a phase-object described by a single complex 2D transmission function. In contrast, multislice ptychography adopts the inverse of the multislice simulation formalism, reconstructing a stack of complex-valued object slices along the beam direction from the set of diffraction patterns for each tilt[52–54,62]. Both reconstruction modes employed the maximum likelihood method, using the parameters listed in Extended Data Table 2. Step sizes for both the probe and the object updates were optimized to ensure convergence while avoiding overfitting to noise. Unlike simulated ADF images, which remain aligned as long as the atomic model is consistent across tilt angles, the reconstructed phase images can exhibit relative shifts between tilts. This misalignment arises from the simultaneous

updates of both the probe and object functions during reconstruction. As a result, even in simulations, careful alignment of the phase images across tilt angles is required. Finally, to account for partial coherence, the single-slice and multislice reconstructions were convolved with a 0.35 Å Gaussian kernel, and the resulting projections were used as input to the AET workflow described in Table 1.

Data availability

All data supporting this study are publicly available on GitHub (github.com/AET-pAET/Supplementary-Data-Codes) and archived on Zenodo at https://doi.org/10.5281/zenodo.17445110 (ref. 63).

Code availability

All source codes used for preprocessing, denoising, projection alignment and normalization, tomographic reconstruction, atom tracing, elemental classification, atomic position refinement, ptychographic reconstruction, and data analysis in this study are publicly available on GitHub (github.com/AET-pAET/Supplementary-Data-Codes) and archived on Zenodo at https://doi.org/10.5281/zenodo.17445110 (ref. 63).

58. Cowley, J. M. & Moodie, A. F. The scattering of electrons by atoms and crystals. I. A new theoretical approach. *Acta Crystallogr.* **10**, 609–619 (1957).
59. Goodman, P. & Moodie, A. F. Numerical evaluations of N-beam wave functions in electron scattering by the multi-slice method. *Acta Crystallogr. A* **30**, 280–290 (1974).
60. Miao, J., Sayre, D. & Chapman, H. N. Phase retrieval from the magnitude of the Fourier transform of nonperiodic objects. *J. Opt. Soc. Am. A* **15**, 1662–1669 (1998).
61. Wakonig, K. et al. PtychoShelves, a versatile high-level framework for high-performance analysis of ptychographic data. *J. Appl. Crystallogr.* **53**, 574–586 (2020).
62. Tsai, E. H. R., Usov, I., Diaz, A., Menzel, A. & Guizar-Sicairos, M. X-ray ptychography with extended depth of field. *Opt. Express* **24**, 29089–29108 (2016).
63. University of California, Los Angeles. Supplementary-data-codes. *Zenodo* https://doi.org/10.5281/zenodo.17445110 (2025).

Acknowledgements This work was primarily supported by STROBE, a National Science Foundation Science and Technology Center, under award DMR-1548924. C.M.O. and H.Z. acknowledge support from the US Air Force Office of Scientific Research Multidisciplinary University Research Initiative (MURI) under award FA9550-23-1-0281. Multislice simulations and ptychographic reconstructions were performed at the National Energy Research Scientific Computing Center (NERSC), a Department of Energy User Facility using NERSC awards BES-ERCAP34513 and ERCAP28035.

Author contributions J.M. directed the project. Y.L., Y.Y., C.M.O., H.S. and J.M. discussed and/or performed numerical simulations, 3D reconstruction, atom tracing and classification and data analysis for ADF-based AET. Y.L., H.S., C.M.O., H.Z. and J.M. discussed and/or conducted numerical simulations, phase retrieval, 3D reconstruction, atom tracing and classification and data analysis for pAET. J.M., C.M.O. and Y.L. wrote the paper. All authors commented on the paper.

Competing interests The authors declare no competing interests.

Additional information

Supplementary information The online version contains supplementary material available at https://doi.org/10.1038/s41586-025-09857-4.

Correspondence and requests for materials should be addressed to Jianwei Miao.

Peer review information *Nature* thanks the anonymous reviewer(s) for their contribution to the peer review of this work. Peer reviewer reports are available.

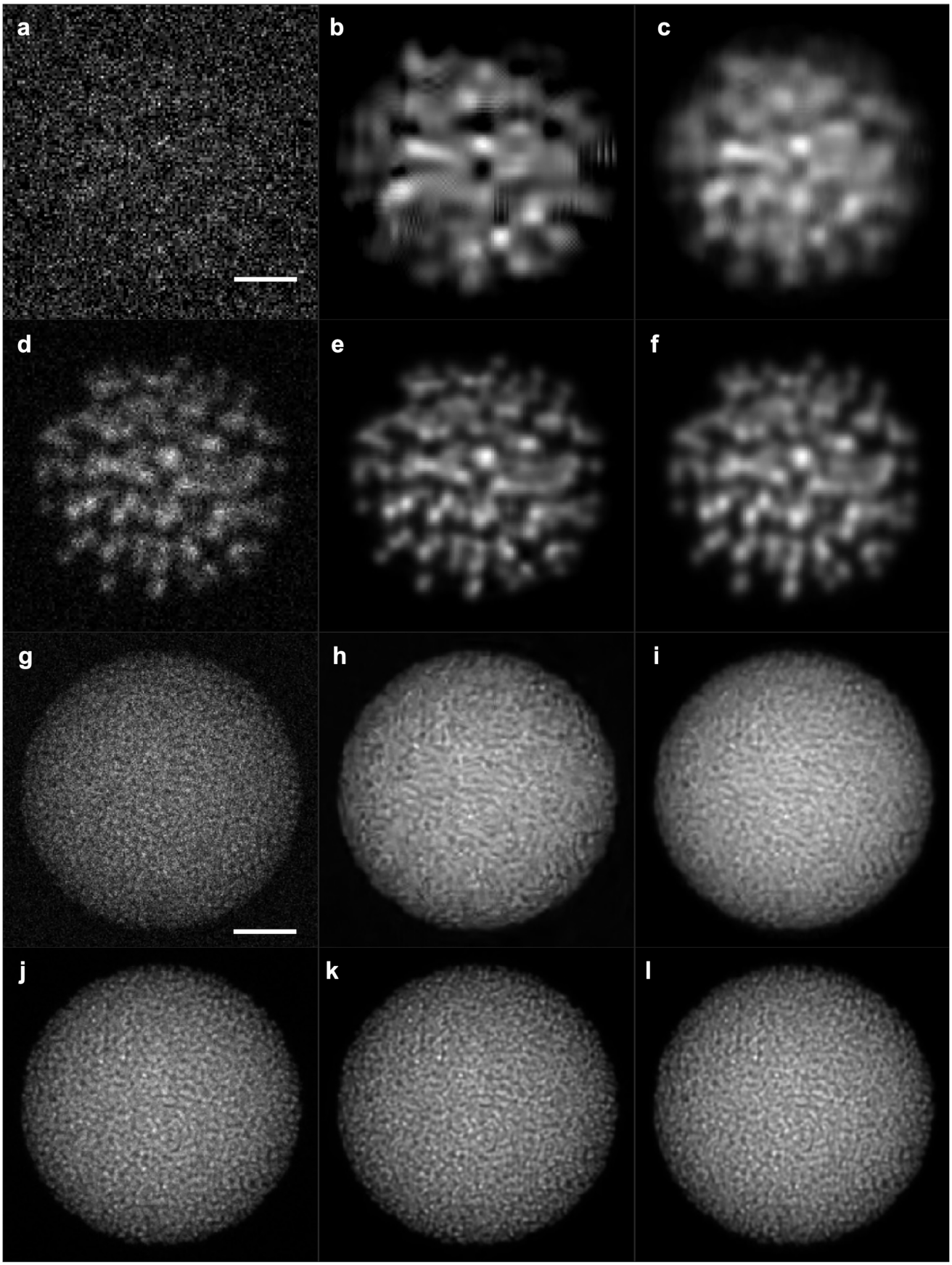

Extended Data Fig. 1 | Projections of 208-atom and 19,993-atom amorphous Si nanoparticles using our AET workflow. a, Representative projection of the 208-atom Si nanoparticle at a dose of 8.0×10^3 $e^-/Å^2$. Scale bar, 5 Å. **b**, Denoised and background-subtracted projection showing residual artifacts due to low signal-to-noise ratio. **c**, Corresponding projection calculated from the RESIRE reconstruction. **d**–**f**, Same as (**a**–**c**) at a dose of 1.6×10^5 $e^-/Å^2$. **g**–**i**, Same as (**a**–**c**) for the 19,993-atom nanoparticle at a dose of 8.0×10^3 $e^-/Å^2$. Scale bar, 2 nm. **j**–**l**, Same as (**g**–**i**) at a dose of 1.6×10^5 $e^-/Å^2$.

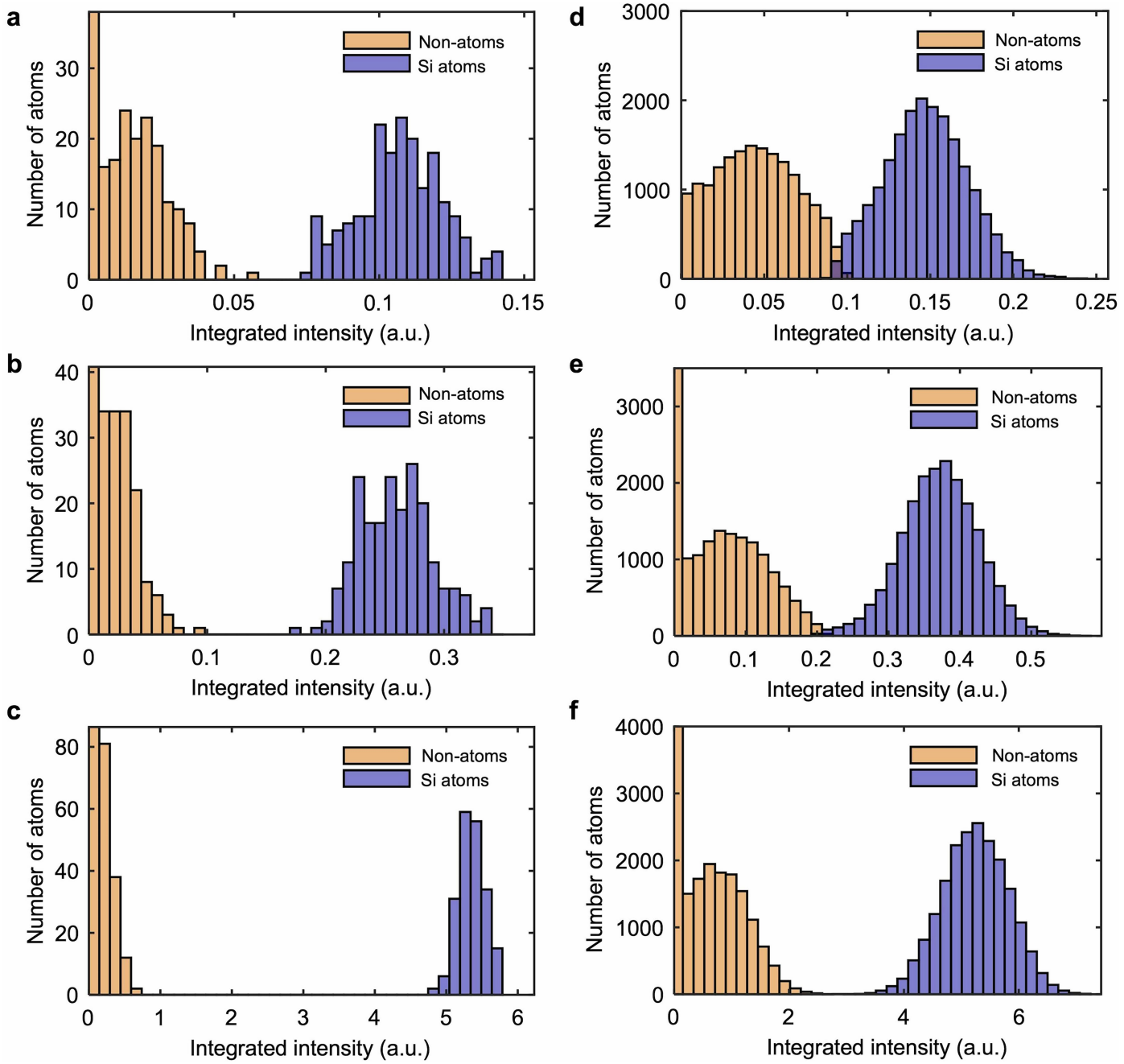

Extended Data Fig. 2 | 3D atomic localization from RESIRE reconstruction using our AET workflow. a-c, Correctly identified Si atoms in the 208-atom nanoparticle: 199 (95.7 %) at 8×10^3 e$^-$/Å^2 (**a**), and 208 (100 %) at both 1.6×10^4 e$^-$/Å^2 (**b**) and 1.6×10^5 e$^-$/Å^2 (**c**). **d-f**, Correctly identified Si atoms in the 19,993-atom nanoparticle: 18,451 (92.3 %) at 8×10^3 e$^-$/Å^2 (**d**), 19,635 (98.2 %) at 1.6×10^4 e$^-$/Å^2 (**e**), and 19,986 (100 %) at 1.6×10^5 e$^-$/Å^2 (**f**).

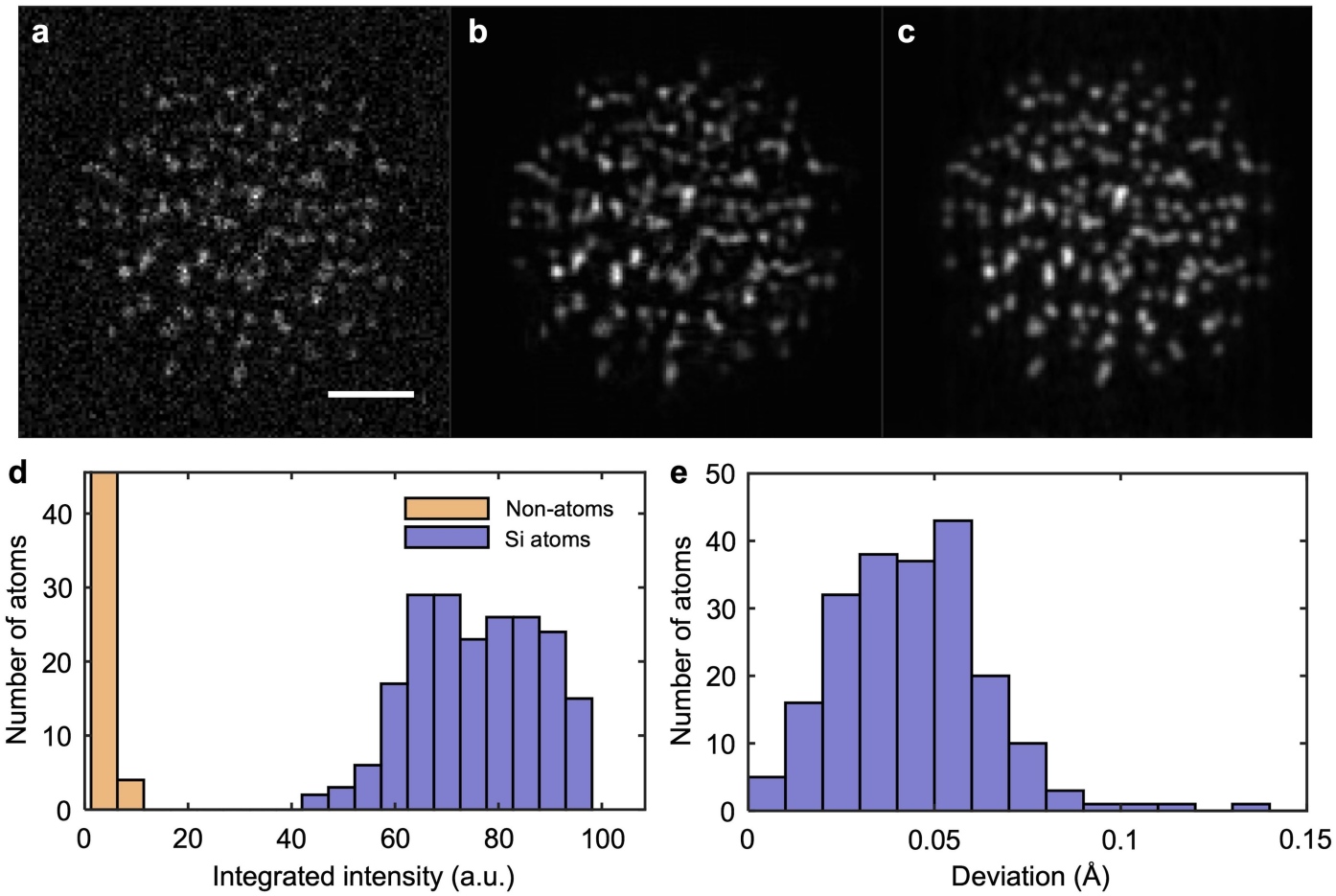

Extended Data Fig. 3 | Improved AET reconstruction of the 208-atom amorphous Si nanoparticle using our workflow applied to simulated projections from ref. 28. a, Representative projection at a dose of 6.6×10^4 $e^-/Å^2$. Scale bar, 5 Å. **b**, Denoised and background-subtracted projection. **c**, Corresponding projection calculated from the RESIRE reconstruction. **d**, All 208 Si atoms correctly identified. **e**, Histogram showing a 3D positional precision of 5 pm.

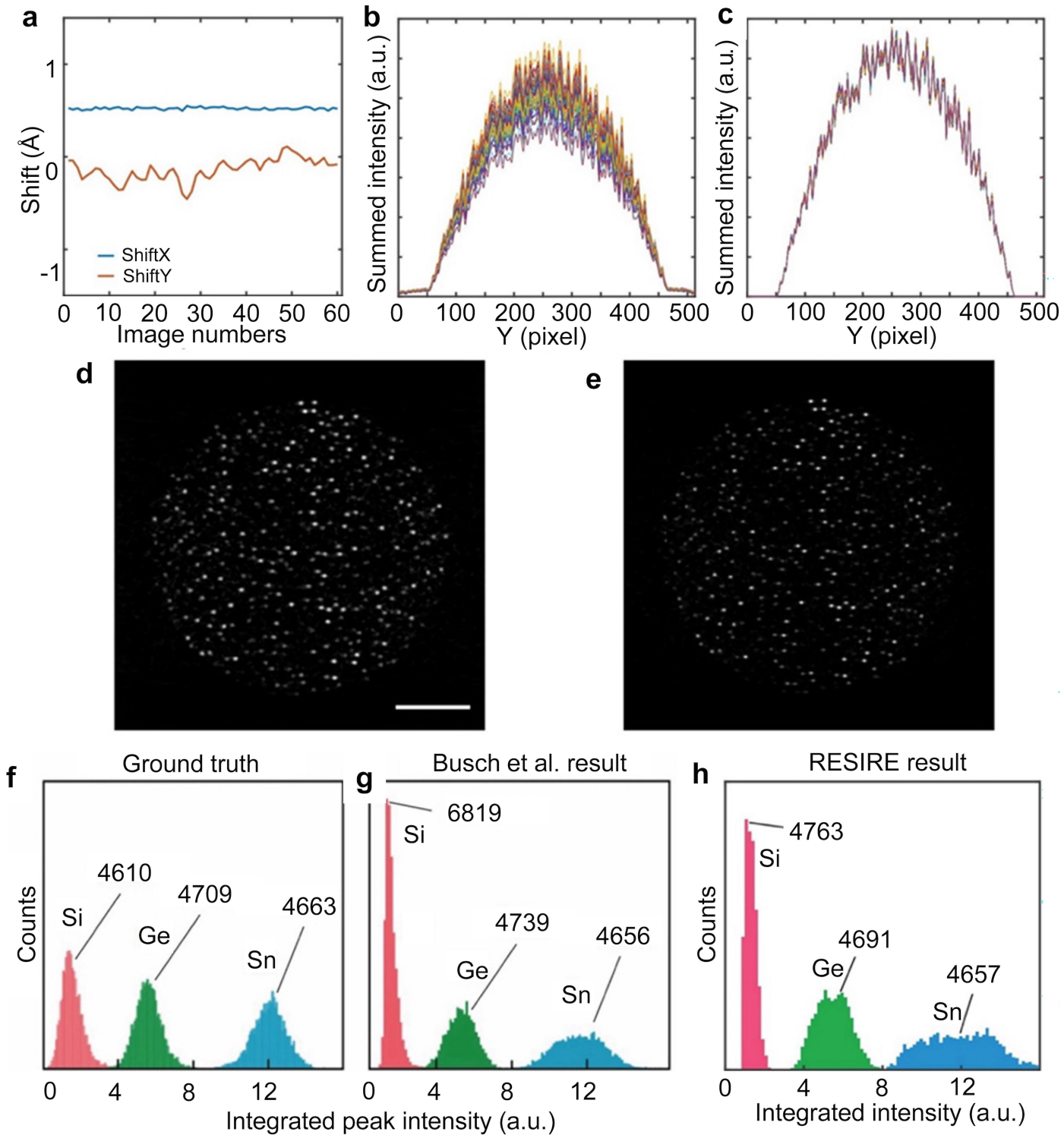

Extended Data Fig. 4 | Improved AET results for the amorphous SiGeSn nanoparticle using our workflow applied to simulated projections from ref. 28. a, Misalignment of projections from ref. 28, particularly along the y-axis. **b**, Common-line analysis indicating intensity mis-normalization. **c**, Projections realigned using the centre-of-mass method and normalized with the common-line approach. **d**, 0.98 Å-thick central slice from the reconstruction reported in ref. 28. Scale bar, 2 nm. **e**, Corresponding slice from our RESIRE reconstruction. **f**, Ground-truth atomic species of the SiGeSn nanoparticle. **g**, Elemental classification of Si, Ge, and Sn as reported in ref. 28. **h**, Elemental classification obtained from our RESIRE reconstruction (**e**). Panels **f** and **g** are adapted from Figure 3b of ref. 28, Springer Nature Limited.

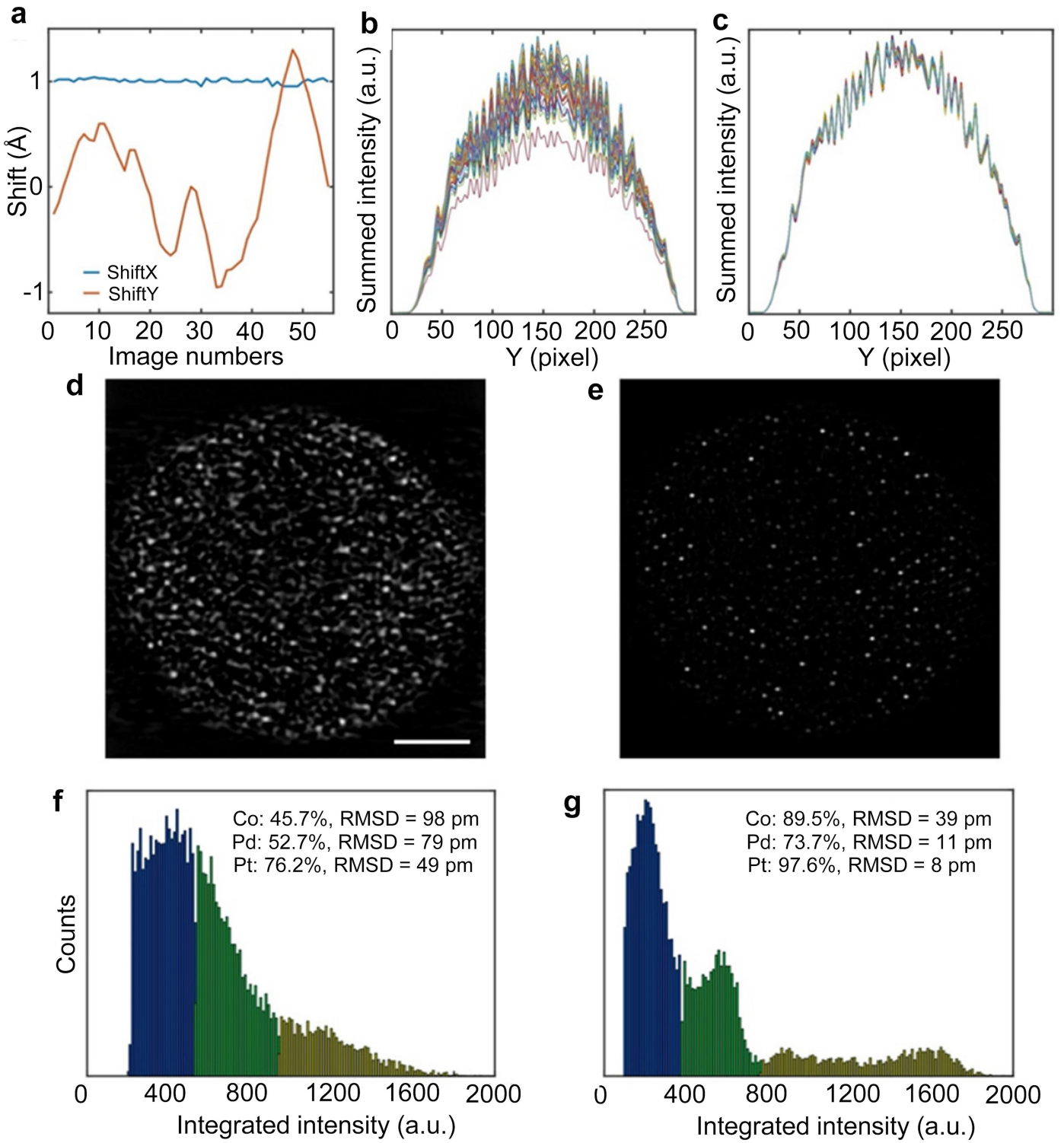

Extended Data Fig. 5 | Projection misalignment and intensity mis-normalization in simulated projections of an amorphous CoPdPt nanoparticle from ref. 28. a, Centre-of-mass analysis showing significant y-axis misalignment in the projections from ref. 28. **b**, Common-line analysis revealing inconsistent intensity normalization. **c**, Projections realigned using the centre-of-mass method and normalized with the common-line approach. **d**, 1 Å-thick central slice from the reconstruction reported in ref. 28. Scale bar, 2 nm. **e**, Corresponding slice from our RESIRE reconstruction. **f**, Histogram of identified atoms generated by applying Busch et al.'s code to their reconstruction in (**d**). **g**, Histogram generated from our RESIRE reconstruction in (**e**).

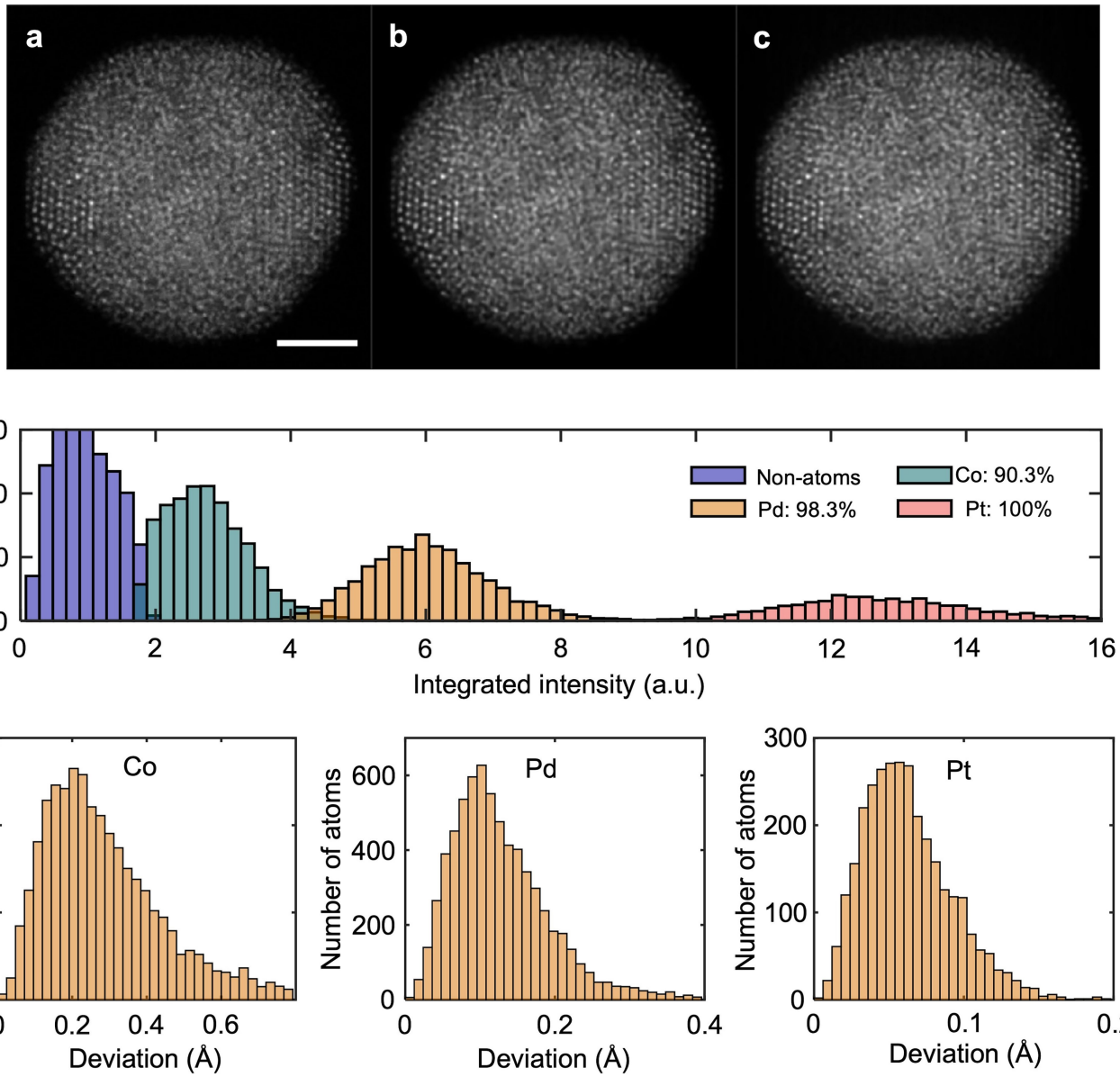

Extended Data Fig. 6 | 3D atomic structure of the amorphous CoPdPt nanoparticle reconstructed with a random defocus range of ±3 nm using our AET workflow. a, Representative projection simulated at a dose of 1.7×10^4 $e^-/Å^2$. Scale bar, 2 nm. **b**, Denoised and background-subtracted projection. **c**, Corresponding projection calculated from the RESIRE reconstruction. **d**, Histogram of traced atoms showing identification accuracies of 90.3% (Co), 98.3% (Pd), and 99.9% (Pt), with an overall accuracy of 95%. **e**, 3D positional precisions of 40 pm (Co), 15 pm (Pd), and 7 pm (Pt); overall precision, 28 pm.

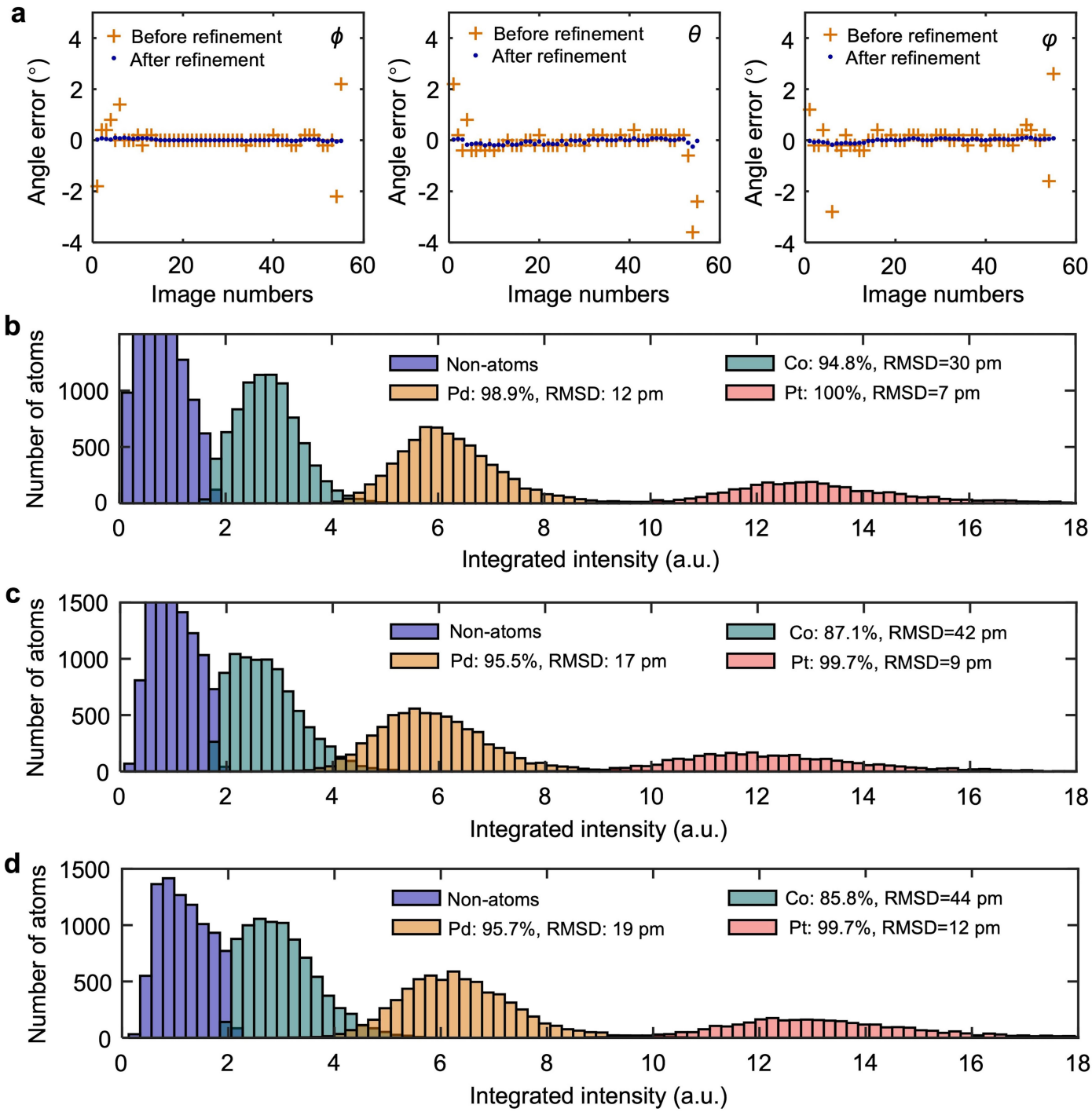

Extended Data Fig. 7 | Quantitative comparison between RESIRE and an updated SIRT under experimentally realistic conditions. Reconstructions were performed using the same simulated noisy projections of the amorphous CoPdPt nanoparticle at a dose of 1.7×10^4 $e^-/Å^2$ as in Fig. 3. **a**, Angular refinement using RESIRE with experimental tilt angles (containing errors) as the initial input. RESIRE successfully refined all three tilt angles (ϕ, θ, and φ). **b**, Histogram of traced atoms from the RESIRE reconstruction showing identification accuracies and 3D positional precisions: 94.8 % and 30 pm for Co, 98.9 % and 12 pm for Pd, and 100 % and 7 pm for Pt. **c**, RESIRE reconstruction without angular correction, achieving 87.1 % and 42 pm for Co, 95.5 % and 17 pm for Pd, and 99.7 % and 9 pm for Pt. **d**, Updated SIRT reconstruction, achieving 85.8 % and 44 pm for Co, 95.7 % and 19 pm for Pd, and 99.7 % and 12 pm for Pt. The results in (**c**) and (**d**) were obtained under identical conditions except for the reconstruction algorithm used.

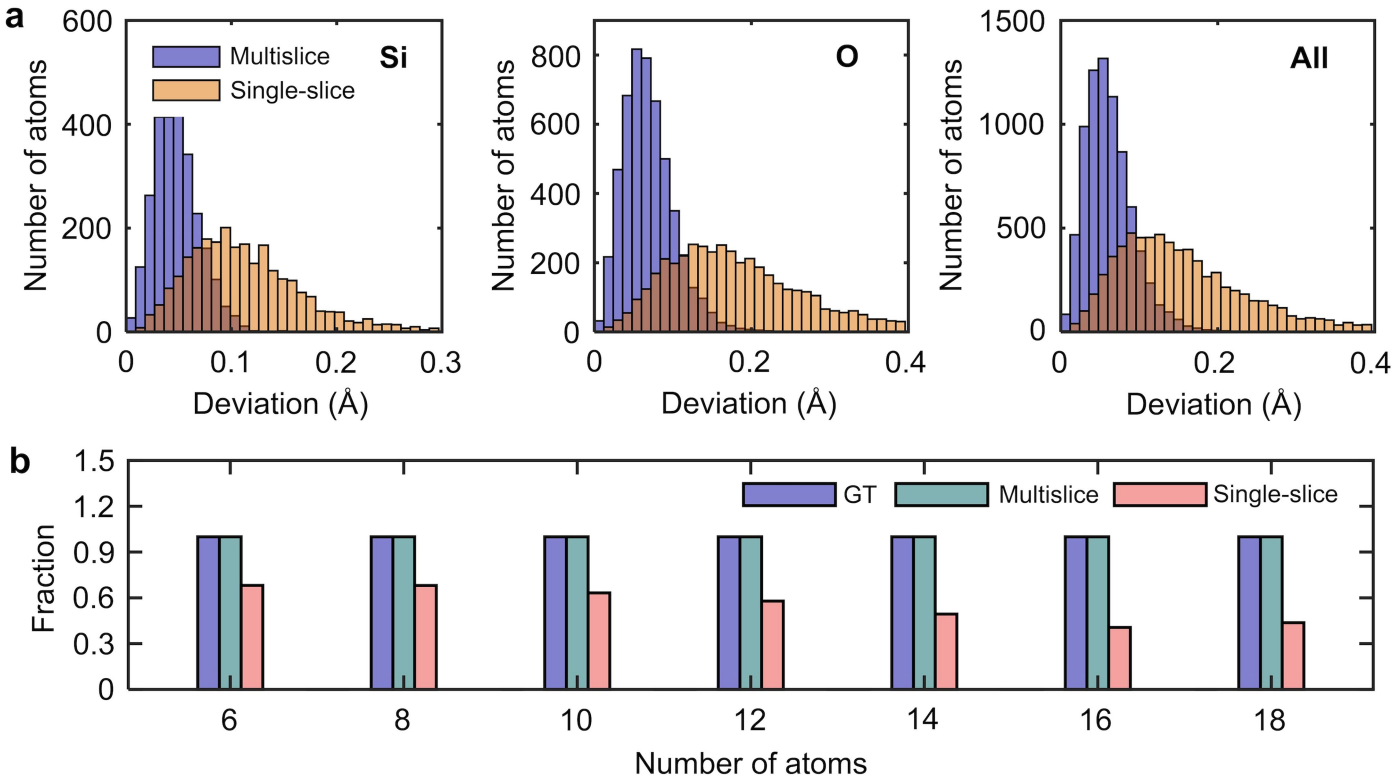

Extended Data Fig. 8 | 3D atomic structure and medium-range order of a 7,704-atom amorphous silica nanoparticle reconstructed by pAET (dose: 1.6×10^4 $e^-/Å^2$). a, Atom identification rates: 96.3% (Si), 85% (O), and 88.8% (all atoms) for single-slice pAET; 100% (Si, O, and all atoms) for multislice pAET. Corresponding 3D positional precisions: 13 pm (Si), 22 pm (O), and 19 pm (all atoms) for single-slice; 5 pm (Si), 8 pm (O), and 7 pm (all atoms) for multislice. **b**, Heteroatomic ring-size distributions from the ground truth, single-slice, and multislice pAET.

Extended Data Table 1 | Parameters used in multislice simulations and RESIRE reconstructions

Atomic model	**Si**[28]	**Si**[28]	**SiGeSn**[28]	**CoPdPt**[25]	**SiO_2**
Number of atoms	208	19,993	Si: 4,610 Ge: 4,709 Sn: 4,663	Co: 8,322 Pd: 6,896 Pt: 3,138	Si: 2,603 O: 5,101
Diameter (nm)	2	9	8	9	6
Voltage (kV)	200	200	200	200	80
Convergence semi-angle (mrad)	17.5	17.5	17.5	25	30
Defocus from centre (nm)	Random (±3nm range)	Random (±3nm range)	Random (±3nm range)	With and without random defocus (±3 nm range)	18
Scan stepsize (Å)	0.195	0.347	0.347	0.347	0.5
Detector collection angle (mrad)	38-190	38-190	38-190	38-190	0-60
Potential sampling	0.065	0.065	0.065	0.065	0.08
Slice thickness (Å)	1	2	2	2	2
# frozen phonons	8	8	8	8	8
Sigma of Gaussian convolution (Å)	0.35	0.35	0.35	0.35	0.35
Tilt range (°)	-90 to +87	-90 to +87	-90 to +87	-69 to +75	-72 to +72
Number of projections	60	60	60	55	49
Dose ($e^-/Å^2$) per projection	8.0×10^3 1.6×10^4 1.6×10^5	8.0×10^3 1.6×10^4 1.6×10^5	1.6×10^4 1.6×10^5	1.7×10^4	1.6×10^3 1.6×10^4
Algorithm	RESIRE (2×2×2 sub-voxels)	RESIRE (2×2×2 sub-voxels)	RESIRE (2×2×2 sub-voxels)	RESIRE (2×2×2 sub-voxels)	RESIRE (2×2×2 sub-voxels)
Number of iterations	200	200	2000	1000	1000

Extended Data Table 2 | Parameters used in single- and multislice ptychographic reconstructions with the foldslice package

Parameter	Maximum likelihood (Single-slice)	Maximum likelihood (Multislice)
Number of scan positions	208×208	208×208
Detector size (pixel)	152×152	152×152
Max collection angle (mrad)	60	60
Compute node	GPU	GPU_MS
Number of probe modes	1	1
Number of iterations	100	100
Noise model	Amplitude likelihood	Amplitude likelihood
beta_LSQ	0.9	0.9
delta_p	0.1	0.1
Layer regularization	N/A	0.5
Number of slices	N/A	5
Slice thickness (nm)	N/A	2
Reconstruction size (pixel)	152×152	152×152
Reconstruction pixel size (Å)	0.345	0.345